What Makes an Annular Mode "Annular"?

Edwin P. Gerber

*Center for Atmosphere Ocean Science, Courant Institute of Mathematical Sciences, New York University,
New York, New York*

David W. J. Thompson

Department of Atmospheric Science, Colorado State University, Fort Collins, Colorado

ABSTRACT

Annular patterns with a high degree of zonal symmetry play a prominent role in the natural variability of the atmospheric circulation and its response to external forcing. But despite their apparent importance for understanding climate variability, the processes that give rise to their marked zonally symmetric components remain largely unclear. Here the authors use simple stochastic models in conjunction with an atmospheric model and observational analyses to explore the conditions under which annular patterns arise from empirical orthogonal function (EOF) analysis of the flow. The results indicate that annular patterns arise not only from zonally coherent fluctuations in the circulation (i.e., "dynamical annularity") but also from zonally symmetric statistics of the circulation in the absence of zonally coherent fluctuations (i.e., "statistical annularity"). It is argued that the distinction between dynamical and statistical annular patterns derived from EOF analysis can be inferred from the associated variance spectrum: larger differences in the variance explained by an annular EOF and successive EOFs generally indicate underlying dynamical annularity. The authors provide a simple recipe for assessing the conditions that give rise to annular EOFs of the circulation. When applied to numerical models, the recipe indicates dynamical annularity in parameter regimes with strong feedbacks between eddies and the mean flow. When applied to observations, the recipe indicates that annular EOFs generally derive from statistical annularity of the flow in the midlatitude troposphere but from dynamical annularity in both the stratosphere and the mid–high-latitude Southern Hemisphere troposphere.

1. Introduction

"Annular" patterns of variability are structures dominated by their zonally symmetric components. They emerge as the leading empirical orthogonal functions (EOFs) of the Northern Hemisphere sea level pressure field (Lorenz 1951; Kutzbach 1970; Wallace and Gutzler 1981; Trenberth and Paolino 1981; Thompson and Wallace 1998, 2000), the Southern Hemisphere zonal-wind and geopotential height fields (Kidson 1988; Karoly 1990; Hartmann and Lo 1998; Thompson and Wallace 2000; Lorenz and Hartmann 2001), the Southern Hemisphere eddy kinetic field (Thompson and Woodworth 2014), the extratropical circulation in a hierarchy of numerical simulations of the atmospheric circulation (e.g., Robinson 1991; Yu and Hartmann 1993; Lee and Feldstein 1996; Shindell et al.

1999; Gerber and Vallis 2007), and aquaplanet simulations of the ocean circulation (Marshall et al. 2007). They are seemingly ubiquitous features in a range of geophysical flows.

Despite their ubiquity in the climate system, one key aspect of annular structures remains open to debate: What gives rise to their marked zonally symmetric components? Does the zonal symmetry of annular structures reflect coherent variations in climate across a range of longitudes? Or does it largely reflect the constraints of EOF analysis (e.g., Dommenget and Latif 2002; Gerber and Vallis 2005)? Consider a long-standing example: the so-called northern annular mode (NAM) emerges as the leading EOF of the NH sea level pressure field (e.g., Thompson and Wallace 2000). It exhibits a high degree of zonal symmetry and its structure implies in-phase variability in climate between the North Atlantic and North Pacific sectors of the hemisphere. But as discussed extensively in earlier papers (e.g., Deser 2000; Ambaum et al. 2001), the two midlatitude centers

Corresponding author e-mail: Edwin P. Gerber, gerber@cims.nyu.edu

of action of the NAM do not exhibit robust correlations on month-to-month time scales. Does the annularity of the NAM arise from dynamic connections between widely separated longitudes that are simply masked by other forms of variability (e.g., Wallace and Thompson 2002)? Or does the annularity arise from the constraints of the EOF analysis (e.g., Dommenget and Latif 2002; Gerber and Vallis 2005; Monahan et al. 2009)?

The purpose of this paper is to revisit the conditions that give rise to annular structures in the leading patterns of variability of the circulation. We will demonstrate that annular patterns can arise from two distinct characteristics of the flow: (i) ''dynamical annularity,'' where variability in the circulation about its mean state exhibits in-phase correlations at all longitudes, and (ii) ''statistical annularity,'' where the statistics of the flow (e.g., the variance, autocorrelation, and spatial decorrelation scale) are similar at all longitudes. Both conditions can give rise to annular-like EOFs that make important contributions to the variability in the circulation. But only the former corresponds to coherent annular motions in the flow. Section 2 explores the impacts of dynamical annularity versus statistical annularity on EOF analysis of output from two simple stochastic models. Section 3 provides theoretical context for interpreting the results of the simple models. Section 4 applies the insights gained from the simple models to the circulation of an idealized general circulation model and observations. Conclusions are provided in section 5.

2. A tale of two annular modes

In the following, we define dynamical annularity as the case where there are positive covariances between all longitudes around the globe; that is,

$$\text{cov}_X(\lambda_1, \lambda_2) = \frac{\sum_{n=1}^{N} X(\lambda_1, t_n) X(\lambda_2, t_n)}{N} > 0 \qquad (1)$$

for all longitudes λ_1 and λ_2. With this notation, we take X to be a generic variable of interest (e.g., geopotential height or eddy kinetic energy), given as an anomaly from its climatological mean. If Eq. (1) is satisfied, there are coherent underlying motions that cause the circulation to vary in concert at all longitudes, and the integrated covariance around the latitude circle provides a quantitative measure of the importance of the dynamical annularity.

We define statistical annularity as the case where the statistics of the flow do not vary as a function of longitude; that is,

$$\text{cov}_X(\lambda_1, \lambda_2) = f(\Delta\lambda), \qquad (2)$$

where $\Delta\lambda = |\lambda_1 - \lambda_2|$ is the absolute distance between the two points. This definition implies that the variance of the flow is uniform [i.e., $f(0)$] and the covariance between any two longitudes depends only on the distance between them, but not where the two points lie relative to the origin (prime meridian). The criteria for dynamical and statistical annularity are not mutually exclusive, and a flow could satisfy both at once. One would only expect Eq. (2) to hold approximately in the presence of realistic boundary conditions, but in section 4 we show the statistics of the observed atmosphere are remarkably annular, particularly in the Southern Hemisphere.

Here we illustrate how statistical annularity can give rise to an annular EOF, even in the case where there is no underlying dynamical annularity in the circulation (i.e., the motions are explicitly local). We consider two one-dimensional stochastic models: $X_1(\lambda, j)$ and $X_2(\lambda, j)$. The details of the models are given in the appendix, but all the necessary statistics of the models are summarized in Fig. 1. In short, both models are random processes in longitude, are periodic over 360°, and have zonally uniform statistics [see Eq. (2)]. The distinction between the models lies in their covariance structures (Fig. 1c). For model X_1, there is explicitly no global correlation: variability at a given location is only correlated with other longitudes over a range of about ±90°. For model X_2 there is a global correlation of 0.1.

Note that since both models have zonally uniform statistics, the covariance structures shown in Fig. 1c are independent of the base longitude used in the calculations. Moreover, they contain all the information needed to characterize the EOFs of the two models; recall that EOFs correspond to the eigenvectors of the covariance matrix $c_{ij} = \text{cov}_X(\lambda_i, \lambda_j)$. When the statistics are uniform, c_{ij} is simply a function of the distance between λ_i and λ_j, as illustrated in Fig. 1c.

The top three EOFs for the two models are shown in Figs. 2a and 2b. By construction (see discussion in the next section), both models exhibit exactly the same EOFs. The first EOF is perfectly annular, as the analytic formulation of the model allows us to take the limit of infinite sampling. As seen in Fig. 2c, the first EOF also explains exactly the same fraction of the variance in each model: 20%. The second and third EOFs characterize wavenumber-1 anomalies: all higher-order EOFs come in sinusoidal pairs, increasing in wavenumber. The phase is arbitrary, as the two wavenumber-1 modes explain the same fraction of variance. For finite sampling, one would see slight mixing between the wavenumbers, but the top modes are well established, even for a reasonable number of samples.
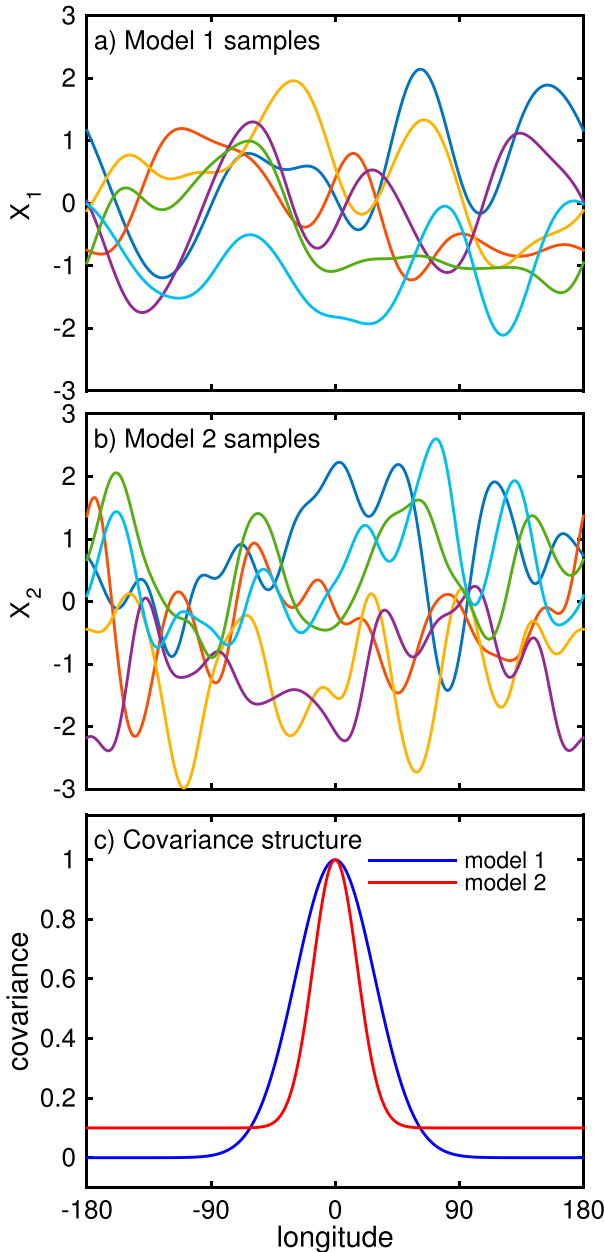
FIG. 1. Two stochastic models of variability in longitude. Sample profiles from models (a) X_1 and (b) X_2. The profiles are independently and identically sampled from the respective distribution of each model, but could be interpreted as different realizations in time, chosen over an interval sufficiently large for the flow to lose all memory from one sample to the next. The y axes are unitless, as each model has been designed to have unit variance. (c) Each model's $\text{cov}_X(0, \lambda)$, the covariance between variability at each longitude with that at $\lambda = 0$. As the statistics are annular, the covariance structure can be fully characterized by this one sample; that is, $\text{cov}_X(\lambda_1, \lambda_2) = \text{cov}_X(0, |\lambda_1 - \lambda_2|)$.
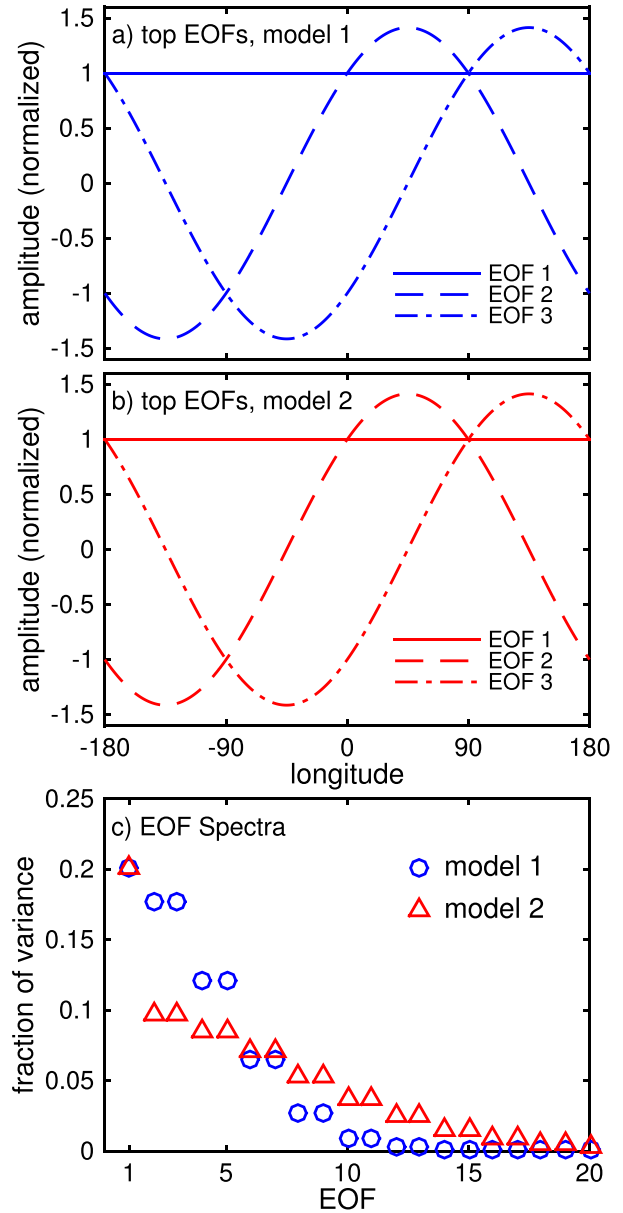

FIG. 2. The EOF structure of the two stochastic models. The top three EOFs for (a) model 1 and (b) model 2, normalized to have unit variance. In the limit of infinite sampling, the EOF patterns from the two models are identical. (c) The models' EOF spectra, marking the fraction of the total variance associated with each of the top 20 EOFs.

The key result in Fig. 2 is that both models exhibit a robust "annular mode" as their leading EOF and that both annular modes explain the same total fraction of the variance. Only one of the apparent annular modes, however, reflects dynamical annularity in the flow.

From the perspective of EOFs, one can only distinguish the two models by examining their EOF spectra—that is, the relative variance associated with all modes

(Fig. 2c). By design, the annular modes (the leading EOFs) in both models explain the same fraction of the total variance (20%). The key differences between the EOF spectra from the two models lie in the relative variance explained by their higher-order EOFs. In the case of model 1, the first EOF explains only slightly more variance than the second or third EOFs. In the case of model 2, there is a large gap between the first and second EOFs. It is the relative variance explained that provides insight into the relative importance of statistical versus dynamical annularity in giving rise to an annular-like leading EOF.

The stochastic models considered in Figs. 1 and 2 highlight two key aspects of annular modes. First, the models make clear that identical annular-like patterns can arise from two very different configurations of the circulation: (i) cases where the statistics of the flow are zonally uniform but the correlations are explicitly local (model 1) and (ii) cases with in-phase variability between remote longitudes (model 2). Second, the models make clear that the spectra of variance yields insight into the role of dynamical annularity in driving the leading EOF.

3. Theoretical insight

For systems with statistical annularity, as in models X_1 and X_2, the EOFs can be entirely characterized based on the covariance structure $f(\Delta\lambda)$. Batchelor (1953) solved the EOF problem for cases with zonally uniform statistics in his analysis of homogeneous, isotropic turbulence in a triply periodic domain. Our discussion is the 1D limit of this more comprehensive analysis. If the statistics are zonally uniform (i.e., homogeneous), then EOF analysis will yield a pure Fourier decomposition of the flow. All EOFs will come in degenerate pairs expressing the same fraction of variance, except for the single wavenumber-0 (annular) mode.

The ordering of the Fourier coefficients depends on the Fourier decomposition of f. The covariance function $f(\Delta\lambda)$ is defined for $0 \leq \Delta\lambda \leq \pi$, where we express longitude in radians. The variance associated with a mode of wavenumber k is then given by

$$\mathrm{var}(k) = \frac{1}{\pi} \int_0^\pi f(\lambda) \cos(k\lambda)\, d\lambda. \tag{3}$$

For all k other than 0, there will be two modes, each characterizing this amount of variance.

Setting $k = 0$ in Eq. (3) shows that the integral of the covariance function determines the variance associated with the annular mode. If we normalize the covariance function by $f(0)$ to obtain the correlation, the integral in

turn provides the relative variance. For systems with zonally uniform statistics, there is thus a nice interpretation of the strength of the annular mode: the fraction of the variance expressed by the annular mode is simply the "average" of the correlation function between a given base point and all other points. This will hold even in cases where the annular mode is not the first EOF.

Returning to the simple stochastic models in section 2, we can now see how the two models were designed to have the same annular mode. Given that the variance at each grid point was set to 1 by construction, the covariance functions are equivalent to the correlation functions. The average correlation in Fig. 1c is 0.2 in both cases, so that the annular mode in each model explains 20% of the total variance. In model X_1, the average correlation of 0.2 derives solely from the strong positive correlation over half a hemisphere. That is, the annular mode is the most important EOF, but it only reflects the annularity of the statistics. In model X_2, half of the variance associated with the annular mode can be attributed to dynamical annularity, as given by the global baseline correlation of 0.1. The other half is attributable to the positive correlation on local scales, reflecting the spatial redness of the circulation.

Model X_2 shows that even in a system with dynamical annularity, the "strength" of the annular model is enhanced by the spatial redness of the flow, which exists independent of underlying dynamical annularity. The weaker spatial redness of the flow in model X_2 relative to X_1 is visibly apparent in the structure of its samples (cf. Figs. 1a and 1b), while the presence of coherent dynamical annularity leads to the large gap between the fraction of variance associated with wavenumber 0 and other waves in the EOF spectrum in Fig. 1c. It follows that an annular EOF is more likely to reflect dynamical annularity when there is large separation between the variance explained by it and higher-order modes. In this case, the average correlation over all longitudes arises from far-field correlation and not simply the local positive correlations associated with the spatial redness of the circulation.

The models in section 2 are two examples from a family of stochastic systems with spatial correlation structure

$$f(\lambda) = (1-\beta)e^{-(\lambda/\alpha)^2} + \beta, \tag{4}$$

illustrated graphically in Fig. 3a. The parameter α is the spatial decorrelation scale (defined as the Gaussian width of the correlations in units of radians) and parameter β is the baseline annular correlation of the model. For systems with this spatial decorrelation
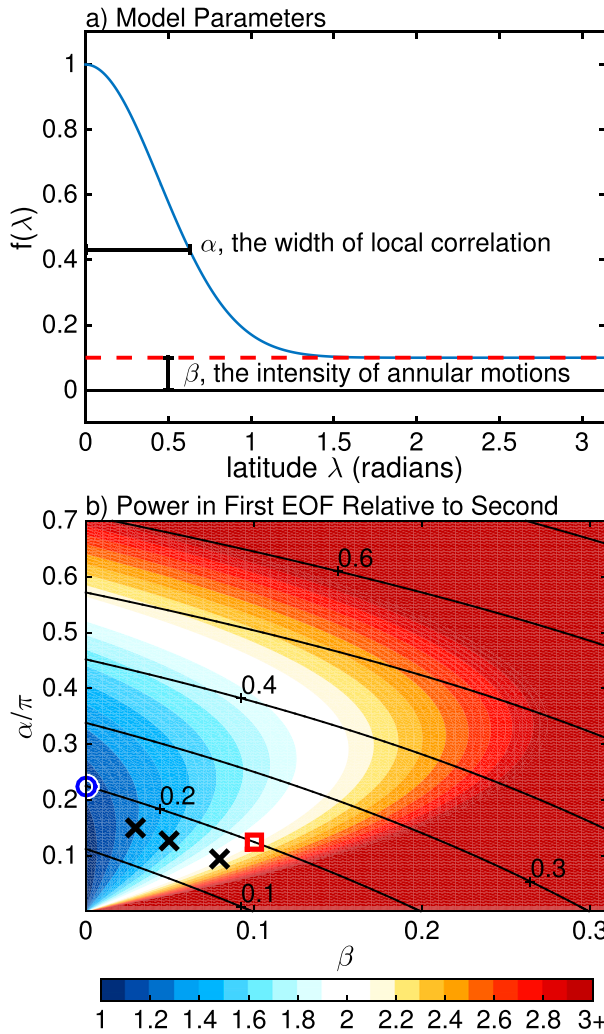
FIG. 3. The impact of local vs annular correlation in the "Gaussian + baseline" family of stochastic models. (a) The parameters α and β, which characterize the correlation function $f(\lambda)$ for each model. (b) The variance expressed by the first EOF (black contours) and the ratio of the variance expressed by the first EOF to that of the second (color shading) as a function of α and β. The first EOF is always annular and the second always a wavenumber-1 pattern. The blue and red markers show the location of models X_1 and X_2 (illustrated in Figs. 1 and 2) in parameter space, respectively; both fall along the same black contour, as their top EOF expresses 0.2 of the total variance. The black crosses will be discussed in the context of Fig. 11.

structure, the leading EOF is always annular and the second and third EOFs always have wave-1 structure, even if there is no annular correlation (i.e., $\beta = 0$). This follows from the fact that a Fourier transform of a Gaussian is a Gaussian, such that power is always maximum at zero and decays with higher wavenumbers.

Figure 3b summarize the variance explained by the leading EOFs of the system considered in Fig. 3a as a function of the spatial decorrelation scale (ordinate) and

the amplitude of the baseline annular correlation (abscissa). The contours indicate the variance explained by the leading (annular) EOF; the shading indicates the ratio of the variance between the leading and second (wavenumber 1) EOFs. Dark blue shading indicates regions where the EOFs are degenerate (explain the same amount of variance). White shading indicates regions where the first EOF explains about twice the variance of the second EOF.

At the origin of the plot ($\alpha \to 0$ and $\beta = 0$), the system approaches the white noise limit, and all EOFs become degenerate. Traveling right along the x axis from the origin (i.e., keeping the spatial decorrelation scale α infinitesimally small and increasing the baseline annular correlation with β), we find that the variance associated with the wavenumber-0 annular mode is simply given by the value of β. Here the spatial decorrelation scale collapses to a single longitude, so all higher modes are degenerate, and the strength of the annular mode derives entirely from dynamical annularity.

If one instead travels upward from the origin, allowing α to increase but keeping $\beta = 0$, the strength of the annular mode increases as well, despite their being no dynamical annularity. These are systems where the annular mode only reflects the annularity of the statistics, not annularity of the motions. As α gets increasingly large, positive correlations will develop at all longitudes by virtue of the fact that the spatial decorrelation scale is longer than a latitude circle. At this point, the spatial redness of the atmospheric motions gives rise to a baseline annular correlation owing to the relatively short length of the latitude circle. When the spatial redness of the flow exceeds half of a latitude circle (0.5 on the ordinate axis), then the variance of the leading (annular) EOF explains approximately twice the variance of the second (wavenumber 1) EOF.

Model 1 sits in the blue shaded region along the ordinate (see blue circle in Fig. 3b), with a spatial decorrelation scale of approximately 0.23 radians. Model 2 (the red square) was designed to have baseline annular correlation of 0.1 (i.e., $\beta = 0.1$), but with an annular mode that express the same fraction of variance, requiring a local correlation $\alpha \approx 0.13$ radians.

The simple models considered in this and the previous section provide insight into the conditions that give rise to annular EOFs and to the importance of the variance explained by the leading EOFs in distinguishing between statistical and dynamical annularity. In the following sections we apply these insights to output from a general circulation model and observations. In the case of complex geophysical flows with out-of-phase correlations between remote longitudes (i.e., teleconnections), one must consider not only the variance

explained by the leading EOFs, but also the spatial correlation structure $f(\Delta\lambda)$.

4. The annularity of the circulation in models and reanalysis

How does the balance between dynamical versus statistical annularity play out in general circulation models and observations? In this section, we apply the insights gained from the simple models to longitudinal variations of the atmospheric circulation at a single latitude—for example, variations in sea level pressure or geopotential height at 50°S. We focus on a single latitude to provide a direct analog to the simple one-dimensional stochastic models in previous sections, albeit a single latitude serves as a stiff test for annular behavior. The northern and southern annular mode patterns are based on EOF analysis of two-dimensional SLP or geopotential height fields, where spherical geometry naturally connects the circulation at all longitudes over the pole.

a. Annular variability in a dry dynamical core

We first consider a moisture-free, three-dimensional primitive equation model on the sphere, often referred to as a dry dynamical core. The model is run with a flat, uniform lower boundary, so that all the forcings are independent of longitude. Hence the circulation is statistically annular, making it an ideal starting point to connect with the theory outlined in the previous section.

The model is a spectral primitive equation model developed by the Geophysical Fluid Dynamics Laboratory (GFDL), run with triangular truncation 42 (T42) spectral resolution and 20 evenly spaced σ levels in the vertical. It is forced with Held and Suarez (1994) "physics," a simple recipe for generating a realistic global circulation with minimal parameterization. Briefly, all diabatic processes are replaced by Newtonian relaxation of the temperature toward an analytic profile approximating an atmosphere in radiative–convective equilibrium, and interaction with the surface is approximated by Rayleigh friction in the lower atmosphere. The equilibrium temperature profile is independent of longitude and time, so there is no annual cycle.

A key parameter setting the structure of the equilibrium temperature profile is the temperature difference between the equator and pole, denoted $(\Delta T)_y$ by Held and Suarez (1994). As explored in a number of studies (e.g., Gerber and Vallis 2007; Simpson et al. 2010; Garfinkel et al. 2013), the strength of coupling between the zonal-mean jet and baroclinic eddies is sensitive to the meridional structure of the equilibrium temperature profile. A weaker temperature gradient leads to stronger
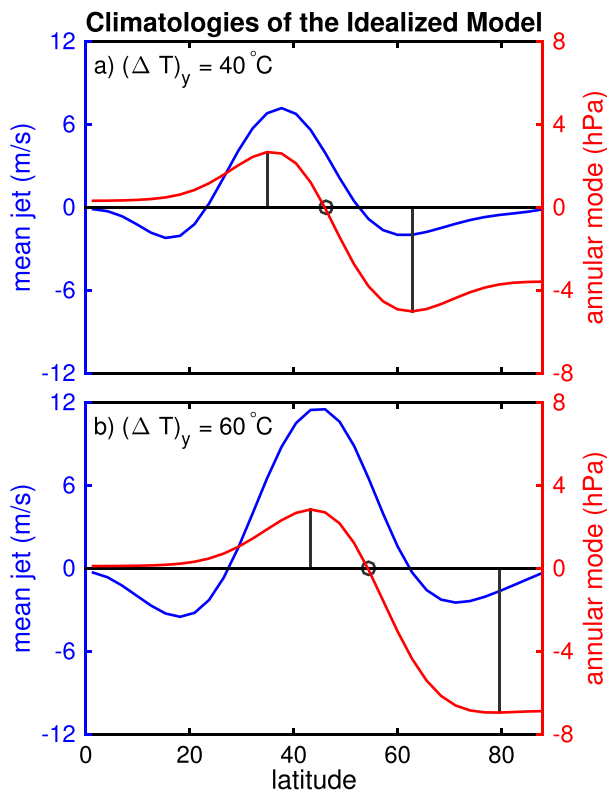

FIG. 4. The mean jet structure and annular modes of the Held and Suarez (1994) model for the $(\Delta T)_y$ = (a) 40° and (b) 60°C integrations. The jet is characterized by the time-mean 850-hPa winds (blue lines, corresponding with the left y axes), and the annular mode is the first EOF of daily, zonal-mean SLP (red, right y axes), normalized to indicate the strength of one-standard-deviation anomalies. The latitudes of the node and equatorward and poleward lobes of the annular mode are highlighted, and correspond with the analysis in Fig. 5.

zonal coherence of the circulation and enhanced persistence of the annular mode. We use this sensitivity to contrast integrations with varying degrees of dynamical annularity.

The temperature difference $(\Delta T)_y$ strongly influences the climatology of the model, as illustrated by the near-surface winds (blue curves) in Fig. 4, and can be compared with similar results based on ERA-Interim (Fig. 6). The results are based on 10 000-day integrations, exclusive of a 500-day spinup. The default setting for $(\Delta T)_y$ is 60°C and drives a fairly realistic equinoctial climatology with jets at 46° latitude in both hemispheres. With a weaker temperature gradient, $(\Delta T)_y$ = 40°C, the jets weaken and shift equatorward to approximately 38°.

The annular modes—defined as the first EOFs of daily zonal-mean SLP—are illustrated by the red curves in in Fig. 4 [the output is normalized by the square root cosine of latitude before computing the EOFs, following
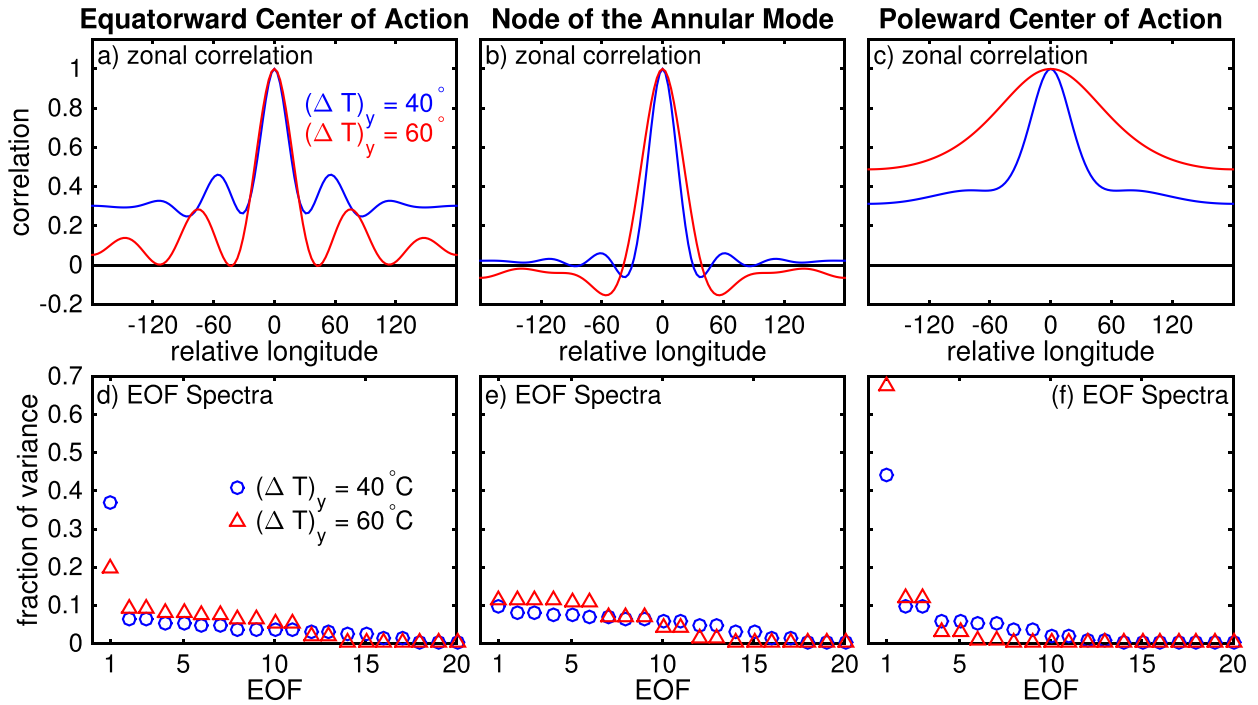
FIG. 5. Characterizing the zonal structure of 10-day pass-filtered SLP anomalies in the Held and Suarez (1994) model. Analysis based at the latitude of the (a),(d) equatorward and (c),(f) poleward centers of action of the annular mode; (b),(e) analysis based at the nodes of the annular mode. (a)–(c) The zonal correlation structure $f(\lambda)$ and (d)–(f) the fraction of variance associated with each of the top 20 EOFs for the integrations with $(\Delta T)_y =$ (a) 40° (blue) and (b) 60°C (red).

Gerber et al. (2008) and Baldwin and Thompson (2009)]. By definition, the positive phase of the annular mode is defined as low SLP over the polar region and thus a poleward shift of the model jet. We use the leading EOFs of SLP to define the annular modes since SLP captures the barotropic component of the flow and is frequently used in previous studies of annular variability (e.g., Thompson and Wallace 2000). In practice, analyses of the near-surface zonal wind field (not shown) yield the same patterns of variability: the first principal component time series associated with the leadings EOFs of zonal-mean SLP and 850-hPa zonal wind are strongly correlated, $R^2 = 0.92$ and 0.88 for $(\Delta T)_y = 40°$ and 60°C, respectively. The centers of action of the annular modes in sea level pressure vary between the two simulations and are indicated by vertical black lines. In the following, we focus our analyses on latitudes corresponding to the centers of action of the annular modes, contrasting it with similar analysis at their nodes.

The top row in Fig. 5 compares the spatial decorrelation structure of sea level pressure anomalies as a function of longitude at these three key latitudes. Results for the integration with weak and standard temperature differences are indicated by blue and red colors, respectively. The bottom row shows the variances explained by the leading EOFs of SLP calculated

along the same latitude bands (i.e., the EOFs are calculated as a function of longitude and time along the indicated latitude bands). We applied a 10-day low-pass Lanczos filter (Duchon 1979) to the data before our analysis to reduce the influence of synoptic-scale variability, but the results are qualitatively similar when based on daily or monthly mean data. To further reduce the sampling uncertainty, the autocorrelation functions were averaged over all longitudes and the EOF spectra were computed directly with Eq. (3). This has the effect of imposing zonally symmetric statistics, which would be the case with infinite sampling, and the results are virtually identical if we use the full fields for the calculations.

We focus first on the equatorward center of action of the annular mode (left column). Variations in sea level pressure in this region are tightly linked with shifts in the midlatitude jet, as evidenced by the high correlation between zonal-mean SLP at this single latitude and the first principal component of zonal-mean zonal wind: $R^2 = 0.95$ and 0.94 for $(\Delta T)_y = 40°$ and 60°C, respectively. The spatial decorrelation scale of SLP anomalies is approximately 60° longitude in both integrations (Fig. 5a). The east–west structure of the correlations reflects the scale of synoptic disturbances and wave trains emanating in both directions. The similarities between the spatial

decorrelation scales reflect the fact that the deformation radius is similar in both runs. The most striking difference between the two runs lies in their baseline annular correlations. In the case of $(\Delta T)_y = 40°C$, the east–west structure of the correlations rides on top of a zonally uniform correlation of approximately 0.3. In the case of the model with $(\Delta T)_y = 60°C$, there is a weaker baseline correlation of approximately 0.1.

The difference in the underlying annularity of the flow explains the differences in the variance spectra shown in Fig. 5d. In both model configurations, the leading EOFs are annular; higher-order modes generally increase monotonically in wavenumber with the exception of waves 5 and 6, which explain larger fractions of the variance that waves 3 and 4, consistent with the synoptic structure of the correlation functions. The distinction between the EOFs between the two model configurations lies in their variance spectra. In the case of $(\Delta T)_y = 40°C$, the annular mode explains more than four times the variance of the second EOF. In the case of $(\Delta T)_y = 60°C$, the annular mode explains about 2 times the variance of the second EOF.

The differences in the variance spectra for the two model configurations are consistent with the theoretical arguments outlined in the previous section. Both model configurations exhibit dynamical annularity, as evidenced by the fact the spatial correlations are >0 at all longitudes. However, the dynamical annularity is much more pronounced for the $(\Delta T)_y = 40°C$ configuration, consistent with the larger ratio in variance explained between the first and second EOFs. The $(\Delta T)_y = 60°C$ configuration is reminiscent of the simple stochastic model X_2, where the leading EOF explains approximately 20% of the variance in the flow: half due to the dynamical annularity; half due to the spatial redness of the flow.

The annularity of flow is notably different along the node of the annular mode, which is strongly linked with variations in the strength of the jet stream. Zonal-mean sea level pressure here is highly correlated with the second EOF of zonal-mean zonal wind, which characterizes fluctuations in the strength and width of the jet (e.g., Vallis et al. 2004): $R^2 = 0.88$ and 0.83 for $(\Delta T)_y = 40°$ and 60°C, respectively. The leading EOFs of SLP along the nodes of the annular modes are again annular, as is the case at the equatorward centers of action (not shown). But along this latitude, there is no apparent baseline annular correlation in either model configuration (Fig. 5b). Accordingly, the EOF variance spectra exhibit little distinction between the variance explained by the first and second EOFs. The enhanced dynamical annularity in the $(\Delta T)_y = 40°C$ case is thus associated chiefly with vacillations of the jet stream's position, not

fluctuations in its strength, which would be reflected by dynamical annularity in SLP at this latitude.

At the minimum of the annular mode pattern on the poleward flank of the jet stream, Figs. 5c and 5f, the relatively small size of the latitude circle leads to a strong baseline annular correlation and thus clear dominance of the annular mode in the variance spectra. The spherical effect is more pronounced for the $(\Delta T)_y = 60°C$ case since the minimum in the EOF pattern is located very close to the pole (Fig. 4). As the length of the latitude circle approaches the scale of the deformation radius, a single synoptic-scale disturbance connects all longitudes, enforcing zonally uniform statistics. While the result appears trivial in this light, this geometric effect may play a significant role in helping the annular mode rise above other modes in two-dimensional EOF analysis. The flow is naturally zonally coherent near the pole, and the tendency for anticorrelation between pressures at polar and middle latitudes may play a role in generating annular-scale motions at lower latitudes (e.g., Ambaum et al. 2001; Gerber and Vallis 2005).

It is important to note that the circulation is more realistic with the default Held and Suarez (1994) setting of $(\Delta T)_y = 60°C$, where the flow exhibits relatively modest zonal coherence at the midlatitude center of action (Fig. 5a). The stronger dynamical annularity in the $(\Delta T)_y = 40°C$ configuration is due to the weak baroclinicity of the jet and the zonally uniform boundary conditions. When zonal asymmetries are introduced to the model, the uniform motions are much reduced, even with weak temperature forcing (Gerber and Vallis 2007). Zonal asymmetries on Earth will thus likely both reduce the strength of globally coherent motions in the sense of Eq. (1) and break the assumption of uniform statistics in the sense of Eq. (2). We find, however, that both dynamical and statistical annularity are highly relevant to flow in reanalysis, at least in the Southern Hemisphere.

b. Annular variability in reanalysis

The data used in this section are derived from the European Centre for Medium-Range Weather Forecasts (ECMWF) interim reanalysis (ERA-Interim; Dee et al. 2011) over the period 1979 to 2013. All results are based on anomalies, where the annual cycle is defined as the long-term mean over the entire 35-yr period. As done for the dynamical core, a 10-day low-pass filter is applied to all data before computing correlations and performing the EOF analyses. Note that qualitatively similar results are derived from daily and monthly mean data.

Figure 6 shows the meridional structures of (i) the climatological zonal-mean zonal wind at 850 hPa and

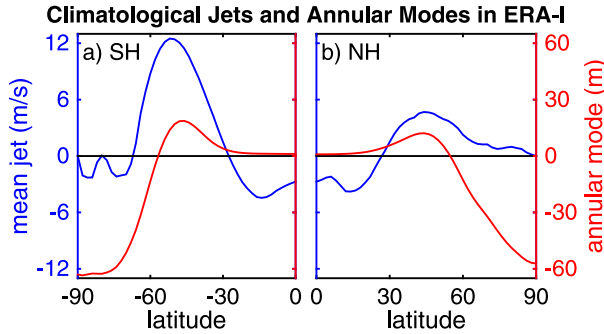## Climatological Jets and Annular Modes in ERA-I

FIG. 6. As in Fig. 4, but for the (a) Southern and (b) Northern Hemispheres in the ERA-Interim, based on the period 1979–2013. To avoid interpolation over mountainous regions, the annular modes are defined in terms of daily, zonal-mean 850-hPa geopotential height (Z_{850}) instead of SLP.

(ii) the southern and northern annular modes. The annular mode time series are defined as the standardized leading PCs of zonal-mean 850-hPa geopotential height (Z_{850}) between 20° and 90° latitude. Since the time series are standardized, the regression patterns shown in Fig. 6 reveal the characteristic amplitude of a one-standard-deviation anomaly in the annular modes. While the long-term mean circulation differs considerably between the two hemispheres, the annular modes are remarkably similar, although the NAM is slightly weaker than the SAM, consistent with the weaker climatological jet. Gerber and Vallis (2005) suggest that the meridional structure of the annular modes tend to be fairly generic, constrained largely by the geometry of the sphere and the conservation of mass and momentum.

The longitudinal correlation structures derived from the observations are not constrained to be uniform with longitude, as is the case for the dry dynamical core. Nevertheless, they are very similar from one base meridian to the next, particularly in the Southern Hemisphere. For example, Fig. 7a shows four single-point covariance maps based on Z_{850} at 50°S: the covariance between Z_{850} at base points 0°, 90°E, 180°, and 90°W with all other longitudes. We have shifted the four regression plots so that the base points overlie each other at the center of the plot. Aside from slight variations in amplitude, there is remarkable uniformity of the east–west correlation structure in the midlatitude Southern Hemisphere circulation: nearly all of the curves collapse upon each other. The correlation structures are positively correlated over a range of approximately ±60° longitude and exhibit alternating negative and positive lobes beyond that point. There is little evidence of global correlation, as is the case with the default Held and Suarez (1994) model.

Figure 7b extends the analysis in the top panel to include averages over all base meridians for geopotential
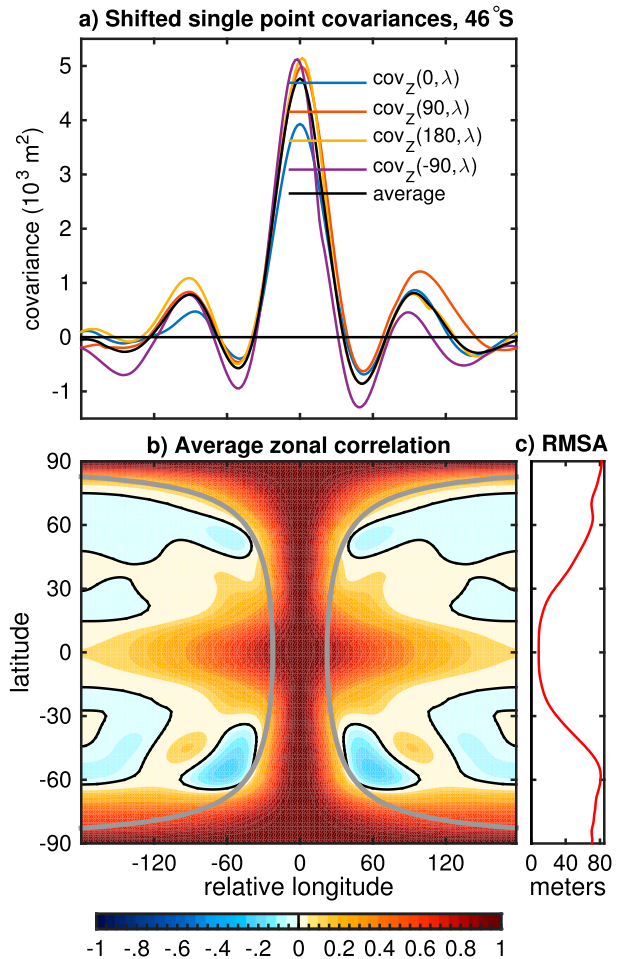

FIG. 7. Characterizing the longitudinal correlation structure of 10-day low-pass-filtered 850-hPa geopotential height in ERA-Interim. (a) Sample single-point correlation maps at 46°S (the equatorward center of action of the SAM), shifted so that base points line up. The black line is the mean of the four curves, an "average single-point correlation map." (b) The average zonal correlation structure of 10-day low-pass-filtered Z_{850} as a function of latitude. The contour interval is 0.05, with black contours marking zero correlation, and gray lines indicate a separation of 5000 km, to provide a sense of geometry on the sphere. (c) The root-mean-square amplitude of 10-day low-pass-filtered Z_{850} anomalies.

data at all latitudes. The figure is constructed as follows: (i) at a given latitude, we calculate the zonal covariance structure for all possible base meridians, as opposed to just four in Fig. 7a, (ii) we then average the resulting covariance structures after shifting them to a common base meridian, (iii) we normalize the resulting "average covariance structure" by the variance to convert to correlation coefficients, and last (iv) we repeat the analysis for all latitudes. The resulting "average correlation structures" for 850-hPa geopotential height are indicated by the shading in Fig. 7b. The black curve
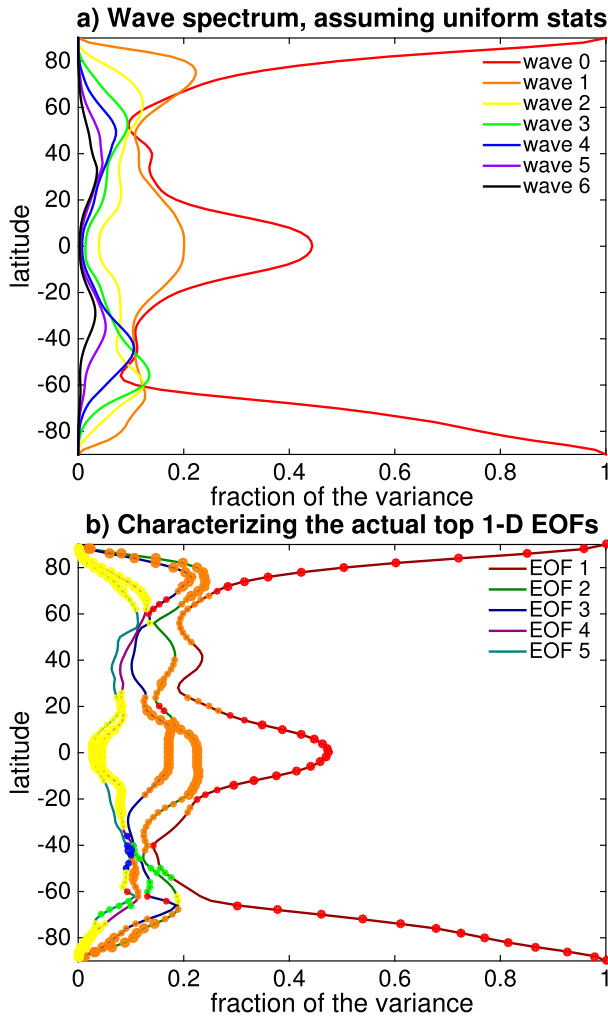
FIG. 8. A comparison of predictions based on zonally uniform statistics to the actual zonal EOF structure of 10-day low-pass-filtered Z_{850}. (a) For each latitude, the fraction of variance associated with wavenumbers 0–6, given the average zonal correlation structure in Fig. 7b and assuming zonally uniform statistics (see text for details). (b) Again for each latitude, the fraction of variance associated with the top five 1D longitudinal EOFs, but now based on the full flow. Large (small) colored dots indicate when a given wavenumber dominates more than 75% (50%) of the power in the EOF, the color identifying the respective wavenumber with the color convention in (a); that is, red = wave 0, orange = wave 1.

denotes the zero contour; the gray curves denote a distance of ±2500 km from the base longitude to provide a sense of the sphericity of Earth. Normalizing the covariance functions by the variance allows us to compare the longitudinal structures in the tropics and the midlatitudes on the same figure; otherwise the increase in the variance of Z_{850} with latitude (illustrated in Fig. 7c) yields much larger amplitudes in the extratropics.

At middle latitudes, positive correlations extend over a distance of approximately 2500 km outward

from the base longitude. Toward the polar regions, the autocorrelations extend over much of the latitude circle owing to the increasingly smaller size of the zonal ring. The austral polar regions are exceptional, in that the correlations extend not only around the circumference of the latitude circle, but also well beyond 2500 km as far equatorward as 60°S. Interestingly, tropical geopotential height is also correlated over long distances. The significant positive correlations at tropical latitudes are robust at most individual longitudes outside of the primary centers of action of ENSO (not shown). The in-phase behavior in tropical geopotential height is consistent with the dynamic constraint of weak pressure gradients at tropical latitudes (Charney 1963; Sobel et al. 2001) and will be investigated further in future work. Note that the amplitude of variations in geopotential height are more than an order of magnitude weaker in the tropics than midlatitudes, as illustrated in Fig. 7c.

The results shown in Fig. 7 are based on 10-day low-pass-filtered data. As discussed in Wettstein and Wallace (2010), large-scale structures in the atmospheric circulation are increasingly prevalent at lower-frequency time scales. Analogous calculations based on monthly mean data (not shown) reveal a slight extension of the region of positive correlations at all latitudes, but overall the results are qualitatively unchanged. Notably, the midlatitude correlation structure is still dominated by alternating negative and positive anomalies beyond 2500 km, with little evidence of zonally coherent motions.

How does the average correlation structure shown in Fig. 7b project onto the EOFs of the circulation? Figure 8 characterizes the (top) "predicted" and (bottom) "actual" EOFs of zonally varying Z_{850} calculated separately for each latitude (e.g., results at 60°N indicate the variance expressed by EOFs of Z_{850} sampled along the 60°N latitude circle). The predicted EOFs are found assuming the statistics of Z_{850} are zonally uniform. In this case, the results of the EOF analysis correspond to a Fourier decomposition of the flow (see discussion in section 3), and the variance captured by each wavenumber is determined by the average correlation structure (Fig. 7b) applied to Eq. (3). Wavenumber-0 (i.e., annular mode) variability emerges as the leading predicted EOF of the flow at virtually all latitudes but explains a much larger fraction of the variance of the flow in the tropics and the polar regions than it does in middle latitudes, where wavenumbers 0, 1, 2, and 3 are of nearly equal importance. The weak amplitude of wavenumber-0 variability in middle latitudes is consistent with the lack of zonally coherent motions in the average correlation structures shown in Fig. 7b.
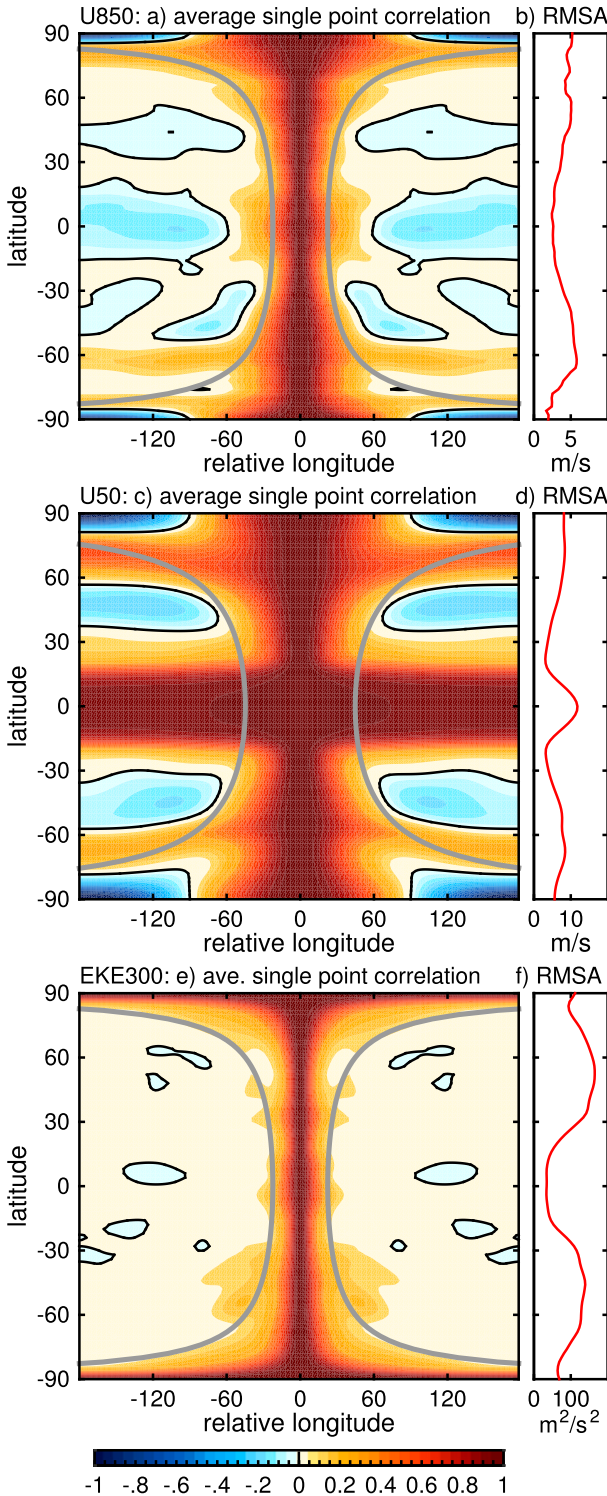
FIG. 9. The average correlation structure of (a) zonal wind at 850 hPa, (c) zonal wind at 50 hPa, and (e) eddy kinetic energy at 300 hPa. As in Fig. 7b, thin black contours mark zero correlation and the thick gray contours give a sense of sphericity, marking a separation of 5000 km as a function of latitude in (a) and (e) and a distance of 10 000 km in (c). (b),(d),(f) The root-mean-square amplitude of variations as a function latitude for each variable, respectively.

The actual EOFs are computed directly from Z_{850} and, thus, do not assume that the statistics of the flow are zonally uniform. Red dots indicate when the EOF is dominated by wavenumber-0 variability, orange dots by wave-1 variability, and so forth for higher wavenumbers. (Note that for the predicted EOFs, all wavenumbers other than 0 include two modes in quadrature that account for equal variance, whereas for the actual EOFs, the two modes associated with each wavenumber are not constrained to explain the same fraction of the variance.) Comparing the top and bottom panels, it is clear that the EOFs predicted from the average correlation structure, assuming zonally uniform statistics, provide useful insight into the true EOFs of the flow. The meridional structures of the variance explained by the leading predicted and actual EOFs are very similar: in the high latitudes and tropics, the first mode is dominated by wavenumber-0 variability and explains a much larger fraction of the flow than EOF 2; in the midlatitudes, the EOFs cluster together and are largely degenerate.

The key point derived from Figs. 7 and 8 is that the "average correlation function" provides a clear sense of where the EOFs of the flow derive from robust dynamical annularity. The circulation exhibits globally coherent motions in the tropics and high latitudes, particularly in the SH high latitudes (Fig. 7), and it is over these regions that the leading EOFs predicted from the average correlation function (Fig. 8a) and from actual variations in the flow (Fig. 8b) exhibit robust wavenumber-0 variability. In contrast, the circulation does not exhibit globally coherent variations at middle latitudes (Fig. 7b), and thus both the predicted and actual EOFs of the flow are degenerate there (Fig. 8). Annular variations in lower-tropospheric geopotential height are consistent with dynamical annularity of the flow in the polar and tropical regions but statistical annularity at middle latitudes.

Figure 9 explores the average correlation structure in three additional fields. Figures 9a,b show results based on the zonal wind at 850 hPa (U_{850}), which samples the barotropic component of the circulation and, thus, emphasizes the eddy-driven jet in middle latitudes. Figures 9c,d are based on the zonal wind at 50 hPa and (U_{50}), which samples both the QBO and variations in the stratospheric polar vortices, and Figs. 9e,f, the eddy kinetic energy at 300 hPa (EKE$_{300}$), which samples the baroclinic annular mode (Thompson and Barnes 2014).

The most pronounced zonal correlations in U_{850} are found in two locations: (i) along 60°S, where positive correlations wrap around the latitude circle, and (ii) in the deep tropics, where positive correlations extend well beyond the 2500-km isopleths. At ~60°S, the zonally
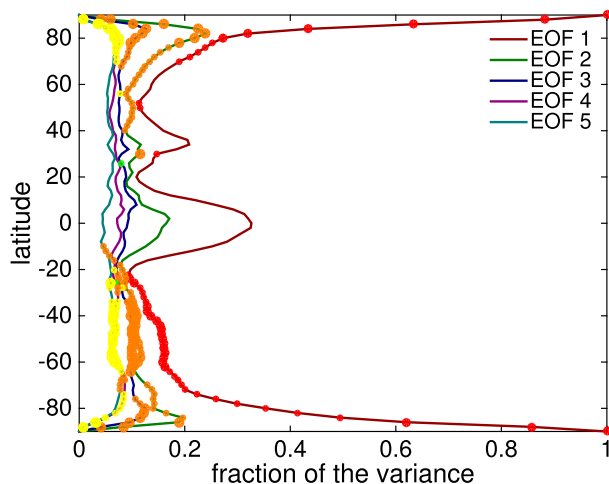
FIG. 10. As in Fig. 8b, but for eddy kinetic energy at 300 hPa. Zonal asymmetry in the statistics lead to substantial mixing between wavenumbers in the Northern Hemisphere (outside the polar cap) and tropics, such that no single wavenumber dominates each EOF. Statistical annularity in the Southern Hemisphere, however, leads to a clearly ordered spectrum poleward of 25°S, dominated by an annular (wavenumber 1) mode at all latitudes.

coherent variations in the zonal flow follow from geostrophic balance and the coherence of the geopotential height field over Antarctica, as observed in Fig. 7b. In the subtropics, the far-reaching correlations follow from geostrophic balance and the coherence of the geopotential height field in the tropics. At the equator, where geostrophic balance does not hold, Z_{850} exhibits globally coherent motions (consistent with weak temperature gradients in the tropics), while U_{850} becomes significantly anticorrelated at a distance. As a result, a zonally uniform annular mode dominates the EOF spectrum of Z_{850} in the tropics (Fig. 8b), whereas wavenumber 1 tends to dominate latitudinal EOF analysis of U_{850} (not shown). Neither Z_{850} (Fig. 7b) or U_{850} (Fig. 9a) exhibit zonally coherent motions at midlatitudes, where the autocorrelation function decays to zero ~2500 km and oscillates in the far field.

The results shown in Figs. 7b and 9a are representative of the correlation structure of geopotential height and zonal wind throughout the depth of the troposphere (e.g., very similar results are derived at 300 hPa; not shown). However, the correlation structure of the zonal flow changes notably above the tropopause, as indicated in Figs. 9c and 9d. Consistent with the increase in the deformation radius in the stratosphere, the scale of motions increases (note that the gray lines now indicate the ±5000-km isopleths). The most notable differences between the troposphere and stratosphere are found in the tropics, where the quasi-biennial oscillation (QBO) leads to an overwhelming annular signal. Marked

annularity is also found in the high latitudes, in the vicinity of both extratropical polar vortices. As observed in the analysis of the tropospheric zonal wind and geopotential height, however, there is no evidence of dynamical annularity in the midlatitudes.

The average correlation structure of EKE_{300} (Fig. 9e) is notably different. Unlike Z or U, the zonal correlation of EKE is remarkably similar across all latitudes, with a slight peak in the physical scale of the correlation in the Southern Hemisphere midlatitudes where the baroclinic annular mode has largest amplitude (e.g., Thompson and Woodworth 2014). Interestingly, EKE_{300} remains positively correlated around the globe at all latitudes, albeit very weakly in the far field. The nonnegative decorrelation structure leads to the dominance of a zonally uniform annular mode in EKE at each individual latitude poleward of 25°S, as shown in Fig. 10. However, the separation between the first and second modes (which characterize wavenumber-1 motions) is modest at most latitudes. The largest separations between the first and second EOFs EKE_{300} are found near 45°, where the top annular EOF represents about 16% of the variance, compared to about 11% for the second and third EOFs.

c. Quantifying the role of dynamical annularity in EKE_{300} with the stochastic model

At first glance, the weak separation between the first and second EOFs of EKE_{300} suggests that much of the annular signal owes itself to local correlations (i.e., statistical annularity). However, a comparison of the EOFs of the observations with those derived from the "Gaussian + baseline" model explored in sections 2 and 3 allows us to be more quantitative about the relative role of dynamical versus statistical annularity in the context of the baroclinic annular mode.

Figure 11 compares the zonal correlation structure (Fig. 11a) and EOF spectrum (Fig. 11b) of the 300-hPa eddy kinetic energy at 46°S, with three fits of the simple stochastic model, each designed to capture key features of the observed behavior. Recall that the model has two parameters: the width of local correlation α and the baseline correlation strength β. As our goal is to focus on the relative role of dynamical annularity, characterized by the difference between the variance expressed by the top EOF (annular mode) and higher-order modes, we remove 1 degree of freedom by requiring that the top EOF express the same fraction of variance in both the simple model and the reanalysis. Hence the first mode explains 16% of the variance for all cases in Fig. 11b. From Eq. (3), this condition is equivalent to keeping the total integral of the correlation structure fixed.
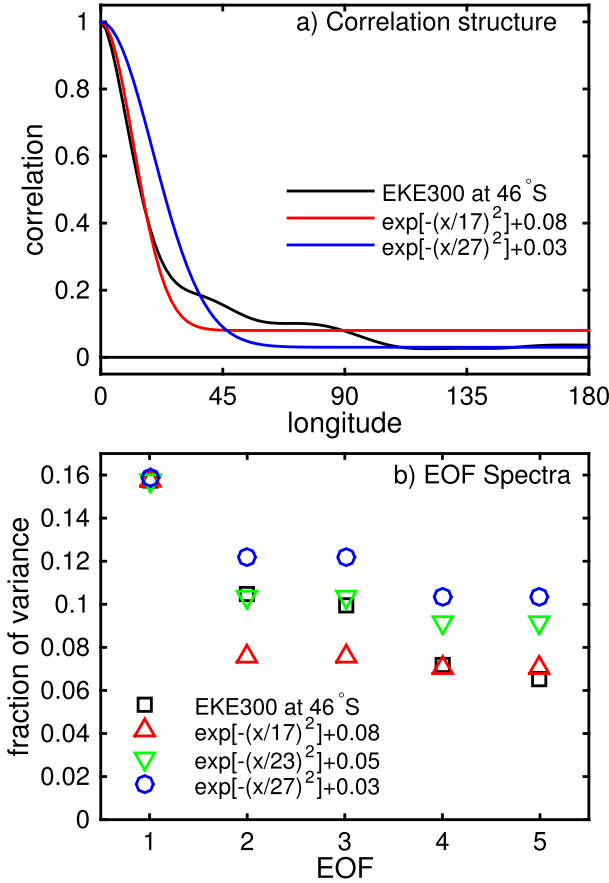
FIG. 11. (a) Comparison between the average longitudinal correlation structure of EKE_{300} at 46°S and two possible fits with the Gaussian + baseline model of section 3. As detailed in the text, the first fit (red) is optimized to capture the initial decay in correlation, while the second fit (blue) is optimized for the long-range correlation baseline. (b) The one-dimensional EOF spectra of EKE_{300} at 46°S, compared against the spectrum for the two fits of the Gaussian + baseline model shown in (a), and a third model with parameters $\alpha = 23°$ and $\beta = 0.05$, as discussed in the text.

In the first fit (red curve, Fig. 11a), we optimize the stochastic model at short range, approximating the fall in local correlation in EKE as a Gaussian with width $\alpha = 17°$. To maintain the variance expressed by the top EOF, parameter β must then be set to 0.08. This choice effectively lumps the midrange shoulder of the EKE_{300} correlation (30°–100°) with the long range (100°–180°), where the observed correlation drops to about 0.03. As a result, the stochastic model exhibits a stronger separation between the first and second EOFs than for EKE_{300} (red triangles versus black squares in Fig. 11b).

An advantage of fitting the data to the simple stochastic model is that it allows us to explicitly quantify the role of dynamical annularity. Since the variance expressed by the annular mode is just the integral of correlation function [Eq. (3)], the contribution of the long-range correlation (dynamical annularity) to the total power of the annular mode is

$$\frac{\int_0^{180} \beta \, d\lambda}{\int_0^{180} [(1-\beta)e^{-(\lambda/\alpha)^2} + \beta] \, d\lambda} \approx \frac{\beta}{\frac{\alpha(1-\beta)\sqrt{\pi}}{360} + \beta}, \quad (5)$$

where we have expressed longitude λ and parameter α in degrees. For the approximation on the left-hand side, we assume that $\alpha \ll 180°$, such that the local correlation does not significantly wrap around the latitude circle. For the "red" model in Fig. 11, dynamical annularity accounts for half of the total strength of the annular mode. Given the fact that it exhibits a stronger separation between the first and second EOFs, however, this is an upper bound on the role of dynamical annularity in EKE_{300} at 46°S.

We obtain a lower bound on the dynamical annularity with the blue fit in Fig. 11a, where the correlation structure is explicitly matched at long range. To conserve the total integral, parameter α in this case must be set to 27°, effectively lumping in the shoulder between 30° and 100° with the local correlation. These parameters would suggest that dynamical annularity contributes only one-fifth of annular mode variance. This is clearly a lower limit, however, as the separation between the first and second EOFs (Fig. 11b) is too small relative to that of EKE_{300}.

Last, we use both degrees of freedom of the stochastic model to find an optimal fit of the EOF spectrum, matching the variance expressed by the top two EOFs (effectively the top three, as higher-order modes come in pairs). The fit, with parameters $\alpha = 23°$ and $\beta = 0.05$, is not shown in Fig. 11a (to avoid clutter), but the resulting EOF spectrum is illustrated by the green triangles in Fig. 11b. With this configuration, dynamical annularity contributes approximately one-third of the annular mode, leaving the remaining two-thirds to statistical annularity associated with the local redness of the EKE. The EOF spectrum of this model diverges from that of EKE_{300} for higher-order modes, such that we should take this as a rough estimate of the true role of dynamical annularity in the baroclinic annular mode.

The location of the three models (lower, optimal, and upper bounds) are marked by the black crosses in Fig. 3b, to put them in context of earlier results. The fits roughly fill in the space between models X_1 and X_2, but on a lower contour where the annular mode expresses 16% of the total variance, as opposed to 20%. The rapid increase in the role of dynamical annularity (from 1/5 to 1/2) matches the rapid ascent in the importance of EOF

1 relative to EOF 2, emphasizing the utility of this ratio as an indicator of dynamical annularity.

5. Concluding remarks

We have explored the conditions that give rise to annular patterns in empirical orthogonal function analysis across a hierarchy of systems: highly simplified stochastic models, idealized atmospheric GCMs, and reanalyses of the atmosphere. Annular EOFs can arise from two conditions, which we term dynamical annularity and statistical annularity. The former arises from zonally coherent dynamical motions across all longitudes, while the latter arises from zonally coherent statistics of the flow (e.g., the variance), even in the absence of significant far-field correlations. Atmospheric reanalyses indicate that both play important roles in the climate system and may aid in the interpretation of climate variability, but only dynamical annularity reflects zonally coherent motions in the circulation.

In general, dynamical annularity arises when the dynamical scales of motion approach the scale of the latitude circle. The average zonal correlation structure (e.g., Fig. 7) thus provides a robust measure of dynamical annularity. In addition, the simple stochastic model suggests that the degree of dynamical annularity in a leading EOF is indicated by the ratio of the variances explained by the first two zonal EOFs of the flow. As a rule of thumb, if the leading annular EOF explains more than twice the variance of the second EOF, then dynamical annularity plays a substantial role in the annular mode. Note, however, that this intuition does not necessarily apply to two-dimensional EOFs in latitude–longitude space, where coherence of meridional variability can lead to dominance of an annular EOF, even when there is explicitly no dynamical annularity (e.g., Gerber and Vallis 2005).

Annular EOFs always—at least partially—reflect statistical annularity of the circulation; zonally coherent motions necessarily imply some degree of zonal coherence. Far-field correlation in the average zonal correlation structure robustly indicates dynamical annularity, but quantification of the statistical annularity requires further analysis: either comparison of the zonal correlation at different base points (e.g., Fig. 7a) or comparison of the predicted and observed zonal EOFs (e.g., Figs. 8 and 10). The localization of the North Pacific and North Atlantic storm tracks limits the utility of the average zonal correlation structure in the Northern Hemisphere troposphere. But the Southern Hemisphere tropospheric circulation is remarkably statistically annular, such that one can predict the full EOF spectrum from the average correlation structure alone.

As discussed in Deser (2000) and Ambaum et al. (2001) and shown here, the observed geopotential height and zonal wind fields do not exhibit robust far-field correlations beyond ~60° longitude in the midlatitudes (i.e., equatorward of roughly 60° latitude). However, the geometry of the sphere naturally favors a high degree of zonal coherence at polar latitudes in both hemispheres, particularly in the geopotential height field. Hence, the northern and southern annular modes do not arise from dynamical annularity in the midlatitude tropospheric circulation but derive a measure of dynamical annularity from the coherence of geopotential height within their polar centers of action. The dynamical annularity of the polar geopotential height field extends to the zonal wind field at high latitudes (~60° latitude) in the Southern Hemisphere, but less so in the Northern Hemisphere. Regions where dynamical annularity plays a seemingly important role in the circulation thus include the following:

 (i) the geopotential height over polar latitudes in both hemispheres, which arises chiefly from the geometry of the sphere;
 (ii) the zonal wind field near 60° latitude in the Southern Hemisphere, which exhibits greater dynamical annularity than would be expected from the geometry of the sphere;
(iii) the tropical geopotential height field, presumably because temperature gradients must be weak in this region (e.g., Charney 1963);
(iv) the tropospheric zonal flow near ~15° latitude; these features arises via geostrophy and the dynamic annularity of the tropical Z field;
 (v) the zonal wind field in the equatorial stratosphere, which reflects the QBO; and
(vi) the eddy kinetic energy in the midlatitude Southern Hemisphere, consistent with the baroclinic annular mode and the downstream development of wave packets in the austral storm track (Thompson et al. 2017). The dynamical annularity of the eddy activity is surprising given the lack of dynamic annularity in the midlatitude barotropic jets, which are intimately connected with eddies through the baroclinic life cycle.

The annular leading EOFs of the midlatitude flow have been examined extensively in previous work, but to our knowledge, the annular nature of tropical tropospheric Z has received less attention. We intend to investigate this feature in more detail in a future study.

of this manuscript. EPG was supported by the National Science Foundation (NSF) through Grant AGS-1546585 and DWJT was supported by the NSF through the Climate Dynamics Program.

APPENDIX

Technical Details of the Stochastic Models

The stochastic models in section 2 are, in a sense, constructed in reverse, starting with the desired result. We begin with the correlation structure f, as shown in Fig. 1c, and project it onto cosine modes as in (3). This gives us the EOF spectra shown in Fig. 2c; that is, how much variance (which we now denote v_k) should be associated with each mode of wavenumber k. Note that not all correlation structures are possible. A sufficient criteria, however, is that the projection of every cosine mode onto f is nonnegative (i.e., all $v_k \geq 0$).

Realizations of the models, as shown in Figs. 1a, 1b, are constructed by moving back into grid space,

$$X(\lambda, j) = v_0^{1/2} \delta_{0,j} + \sum_{k=1}^{\infty} (2v_k)^{1/2} [\delta_{k1,j} \sin(k\lambda) + \delta_{k2,j} \cos(k\lambda)],$$
$$(A1)$$

where all the $\delta_{k,j}$ are independent samples from a normal distribution with unit variance and λ is given in radians. In practice only the top 15 wavenumbers are needed, as the contribution of higher-order modes becomes negligible.

Note that it is possible to construct an infinite number of stochastic systems that have the same correlation structure f. We have taken a simple approach by using the normal distribution to introduce randomness. Any distribution with mean zero could be used, which would impact the variations in individual samples—and so the convergence of the system in j—but not the statistical properties in the limit of infinite sampling.

REFERENCES

Ambaum, M. H. P., B. J. Hoskins, and D. B. Stephenson, 2001: Arctic oscillation or North Atlantic oscillation? *J. Climate*, **14**, 3495–3507, doi:10.1175/1520-0442(2001)014<3495:AOONAO>2.0.CO;2.

Baldwin, M. P., and D. W. J. Thompson, 2009: A critical comparison of stratosphere–troposphere coupling indices. *Quart. J. Roy. Meteor. Soc.*, **135**, 1661–1672, doi:10.1002/qj.479.

Batchelor, G. K., 1953: *The Theory of Homogeneous Turbulence.* Cambridge University Press, 197 pp.

Charney, J. G., 1963: A note on large-scale motions in the tropics. *J. Atmos. Sci.*, **20**, 607–609, doi:10.1175/1520-0469(1963)020<0607:ANOLSM>2.0.CO;2.

Dee, D. P., and Coauthors, 2011: The ERA-Interim reanalysis: Configuration and performance of the data assimilation system. *Quart. J. Roy. Meteor. Soc.*, **137**, 553–597, doi:10.1002/qj.828.

Deser, C., 2000: On the teleconnectivity of the ''Arctic Oscillation.'' *Geophys. Res. Lett.*, **27**, 779–782, doi:10.1029/1999GL010945.

Dommenget, D., and M. Latif, 2002: A cautionary note on the interpretation of EOFs. *J. Climate*, **15**, 216–225, doi:10.1175/1520-0442(2002)015<0216:ACNOTI>2.0.CO;2.

Duchon, C. E., 1979: Lanczos filtering in one and two dimensions. *J. Appl. Meteor.*, **18**, 1016–1022, doi:10.1175/1520-0450(1979)018<1016:LFIOAT>2.0.CO;2.

Garfinkel, C. I., D. W. Waugh, and E. P. Gerber, 2013: The effect of tropospheric jet latitude on coupling between the stratospheric polar vortex and the troposphere. *J. Climate*, **26**, 2077–2095, doi:10.1175/JCLI-D-12-00301.1.

Gerber, E. P., and G. K. Vallis, 2005: A stochastic model for the spatial structure of annular patterns of variability and the NAO. *J. Climate*, **18**, 2102–2118, doi:10.1175/JCLI3337.1.

——, and ——, 2007: Eddy–zonal flow interactions and the persistence of the zonal index. *J. Atmos. Sci.*, **64**, 3296–3311, doi:10.1175/JAS4006.1.

——, S. Voronin, and L. M. Polvani, 2008: Testing the annular mode autocorrelation timescale in simple atmospheric general circulation models. *Mon. Wea. Rev.*, **136**, 1523–1536, doi:10.1175/2007MWR2211.1.

Hartmann, D. L., and F. Lo, 1998: Wave-driven zonal flow vacillation in the Southern Hemisphere. *J. Atmos. Sci.*, **55**, 1303–1315, doi:10.1175/1520-0469(1998)055<1303:WDZFVI>2.0.CO;2.

Held, I. M., and M. J. Suarez, 1994: A proposal for the intercomparison of the dynamical cores of atmospheric general circulation models. *Bull. Amer. Meteor. Soc.*, **75**, 1825–1830, doi:10.1175/1520-0477(1994)075<1825:APFTIO>2.0.CO;2.

Karoly, D. J., 1990: The role of transient eddies in low-frequency zonal variations of the Southern Hemisphere circulation. *Tellus*, **42A**, 41–50, doi:10.1034/j.1600-0870.1990.00005.x.

Kidson, J. W., 1988: Interannual variations in the Southern Hemisphere circulation. *J. Climate*, **1**, 1177–1198, doi:10.1175/1520-0442(1988)001<1177:IVITSH>2.0.CO;2.

Kutzbach, J. E., 1970: Large-scale features of monthly mean Northern Hemisphere anomaly maps of sea-level pressure. *Mon. Wea. Rev.*, **98**, 708–716, doi:10.1175/1520-0493(1970)098<0708:LSFOMM>2.3.CO;2.

Lee, S., and S. B. Feldstein, 1996: Mechanism of zonal index evolution in a two-layer model. *J. Atmos. Sci.*, **53**, 2232–2246, doi:10.1175/1520-0469(1996)053<2232:MOZIEI>2.0.CO;2.

Lorenz, D. J., and D. L. Hartmann, 2001: Eddy–zonal flow feedback in the Southern Hemisphere. *J. Atmos. Sci.*, **58**, 3312–3327, doi:10.1175/1520-0469(2001)058<3312:EZFFIT>2.0.CO;2.

Lorenz, E. N., 1951: Seasonal and irregular variations of the Northern Hemisphere sea-level pressure profile. *J. Meteor.*, **8**, 52–59, doi:10.1175/1520-0469(1951)008<0052:SAIVOT>2.0.CO;2.

Marshall, J., D. Ferreira, J.-M. Campin, and D. Enderton, 2007: Mean climate and variability of the atmosphere and ocean on an aquaplanet. *J. Atmos. Sci.*, **64**, 4270–4286, doi:10.1175/2007JAS2226.1.

Monahan, A. H., J. C. Fyfe, M. H. P. Ambaum, D. B. Stephenson, and G. R. North, 2009: Empirical orthogonal functions: The medium is the message. *J. Climate*, **22**, 6501–6514, doi:10.1175/2009JCLI3062.1.

Robinson, W. A., 1991: The dynamics of low-frequency variability in a simple model of the global atmosphere.

J. Atmos. Sci., **48**, 429–441, doi:10.1175/1520-0469(1991)048<0429:TDOLFV>2.0.CO;2.

Shindell, D. T., R. L. Miller, G. A. Schmidt, and L. Pandolfo, 1999: Simulation of recent northern winter climate trends by greenhouse-gas forcing. *Nature*, **399**, 452–455, doi:10.1038/20905.

Simpson, I. R., M. Blackburn, J. D. Haigh, and S. N. Sparrow, 2010: The impact of the state of the troposphere on the response to stratospheric heating in a simplified GCM. *J. Climate*, **23**, 6166–6185, doi:10.1175/2010JCLI3792.1.

Sobel, A. H., J. Nilsson, and L. M. Polvani, 2001: The weak temperature gradient approximation and balanced tropical moisture waves. *J. Atmos. Sci.*, **58**, 3650–3665, doi:10.1175/1520-0469(2001)058<3650:TWTGAA>2.0.CO;2.

Thompson, D. W. J., and J. M. Wallace, 1998: The Arctic Oscillation signature in the wintertime geopotential height and temperature fields. *Geophys. Res. Lett.*, **25**, 1297–1300, doi:10.1029/98GL00950.

——, and ——, 2000: Annular modes in the extratropical circulation. Part I: Month-to-month variability. *J. Climate*, **13**, 1000–1016, doi:10.1175/1520-0442(2000)013<1000:AMITEC>2.0.CO;2.

——, and E. A. Barnes, 2014: Periodic variability in the large-scale Southern Hemisphere atmospheric circulation. *Science*, **343**, 641–645, doi:10.1126/science.1247660.

——, and J. D. Woodworth, 2014: Barotropic and baroclinic annular variability in the Southern Hemisphere. *J. Atmos. Sci.*, **71**, 1480–1493, doi:10.1175/JAS-D-13-0185.1.

——, B. R. Crow, and E. A. Barnes, 2017: Intraseasonal periodicity in the Southern Hemisphere circulation on regional spatial scales. *J. Atmos. Sci.*, in press.

Trenberth, K. E., and D. A. Paolino, 1981: Characteristic patterns of variability of sea level pressure in the Northern Hemisphere. *Mon. Wea. Rev.*, **109**, 1169–1189, doi:10.1175/1520-0493(1981)109<1169:CPOVOS>2.0.CO;2.

Vallis, G. K., E. P. Gerber, P. J. Kushner, and B. A. Cash, 2004: A mechanism and simple dynamical model of the North Atlantic Oscillation and annular modes. *J. Atmos. Sci.*, **61**, 264–280, doi:10.1175/1520-0469(2004)061<0264:AMASDM>2.0.CO;2.

Wallace, J. M., and D. S. Gutzler, 1981: Teleconnections in the geopotential height field during the Northern Hemisphere winter. *Mon. Wea. Rev.*, **109**, 784–812, doi:10.1175/1520-0493(1981)109<0784:TITGHF>2.0.CO;2.

——, and D. W. J. Thompson, 2002: The Pacific center of action of the Northern Hemisphere annular mode: Real or artifact? *J. Climate*, **15**, 1987–1991, doi:10.1175/1520-0442(2002)015<1987:TPCOAO>2.0.CO;2.

Wettstein, J. J., and J. M. Wallace, 2010: Observed patterns of month-to-month storm-track variability and their relationship to the background flow. *J. Atmos. Sci.*, **67**, 1420–1437, doi:10.1175/2009JAS3194.1.

Yu, J. Y., and D. L. Hartmann, 1993: Zonal flow vacillation and eddy forcing in a simple GCM of the atmosphere. *J. Atmos. Sci.*, **50**, 3244–3259, doi:10.1175/1520-0469(1993)050<3244:ZFVAEF>2.0.CO;2.